



# Breaking through the Cracks: On the Mechanism of Phosphoric Acid Migration in High Temperature Polymer Electrolyte Fuel Cells

J. Halter,<sup>1</sup> F. Marone,<sup>2</sup> T. J. Schmidt,<sup>1,3,\*</sup> and F. N. Büchi<sup>1,\*,z</sup>

<sup>1</sup>Electrochemistry Laboratory, Paul Scherrer Institut, 5232 Villigen PSI, Switzerland

<sup>2</sup>Swiss Light Source, Paul Scherrer Institut, 5232 Villigen PSI, Switzerland

<sup>3</sup>Laboratory of Physical Chemistry, ETH Zürich, 8093 Zürich, Switzerland

In high temperature polymer electrolyte fuel cells, at high current densities, phosphoric acid (PA) migrates toward the anode and invades catalyst, microporous and gas diffusion layers (GDL). This work studies this PA redistribution using synchrotron based operando X-Ray tomographic microscopy (XTM) and electrochemical impedance spectroscopy (EIS) during a current cycling protocol. It is shown that under reformat conditions, during the first 2 minutes after a positive current step, the cell voltage increases due to better wetting of the anode catalyst layer (CL). From 2 to 20 minutes, the cell voltage drops due to increasing mass transport losses in the microporous layer (MPL) and the GDL. At the anode, cracks in MPL and CL, both with widths up to 150  $\mu\text{m}$ , are flooded within 2 minutes after a current density increase. Acid flooding is only observed for MPL cracks that overlap with CL cracks. The CL cracks therefore act as injection points for the flooding of the MPL cracks and the gas diffusion layer. No change in the PA content of any of the cathodic porous components was observed.

© The Author(s) 2018. Published by ECS. This is an open access article distributed under the terms of the Creative Commons Attribution Non-Commercial No Derivatives 4.0 License (CC BY-NC-ND, <http://creativecommons.org/licenses/by-nc-nd/4.0/>), which permits non-commercial reuse, distribution, and reproduction in any medium, provided the original work is not changed in any way and is properly cited. For permission for commercial reuse, please email: [oa@electrochem.org](mailto:oa@electrochem.org). [DOI: 10.1149/2.0501814jes]



Manuscript submitted September 5, 2018; revised manuscript received October 11, 2018. Published October 25, 2018. This was Paper 1380 presented at the Cancun, Mexico, Meeting of the Society, September 30-October 4, 2018.

High temperature polymer electrolyte fuel cells (HT-PEFCs) use a polybenzimidazole membrane, imbibed with phosphoric acid (PA) as electrolyte.<sup>1-4</sup> Unlike PFSA-type membranes, where the conducting group is bound to the base polymer,<sup>5</sup> the bulk of the electrolyte is highly mobile and only a fraction is interacting with the polymer.<sup>6,7</sup> The mobile fraction increases with increasing doping levels of the membrane, as only 2 phosphoric acid molecules per PBI unit interact with the membrane.<sup>8,9</sup> This high degree of mobility allows for a redistribution of phosphoric acid within the membrane electrode assembly (MEA).

This redistribution process does not depend only on MEA material parameters, such as the membrane doping level,<sup>10,11</sup> but is also a function of operation parameters, especially of the current density. Eberhardt et al.<sup>12</sup> showed the invasion of the anode gas diffusion layer (GDL) and the anode flow field after increasing the current density for the first time and were confirmed by similar findings by Becker et al.,<sup>13,14</sup> and Henkensmeier et al.<sup>15</sup> This process of acid redistribution into the anode GDL and flow field channel leads to a loss of phosphoric acid over time. Loss of electrolyte is a major limitation for the lifetime of a HT-PEFC, especially when factoring in the DOE target for combined heat and power applications of 60'000 hours of operation for 2020.

The flooding of the anode GDL is also a concern for the performance of a HT-PEFC due to an increase of anodic mass transport resistance induced by phosphoric acid flooding. A similar problem is known in low temperature PEFC, where liquid water is produced at the cathode. The product water has to be removed through the cathode GDL and it is well known, that this flooding of the cathode is affecting the performance of a LT-PEFC and therefore different research groups are working on this water management issue in LT-PEFC.<sup>16-18</sup>

Such an increasing mass transport was observed by Halter et al.<sup>19</sup> by performing EIS measurements in HT-PEFC under conditions with diluted hydrogen, reflecting reformat operation. They observed an increase in the low frequency regime after a positive current step with a similar time constant, as was observed by Eberhardt et al.<sup>12</sup> with XTM for the GDL flooding.

Common methods for studying phosphoric acid redistribution in operando HT-PEFCs are X-Ray radiography,<sup>20,21</sup> X-Ray tomo-

graphic microscopy (XTM),<sup>11,12</sup> neutron imaging<sup>22</sup> as well as electrochemical methods such as electrochemical impedance spectroscopy (EIS).<sup>19,23-26</sup> Becker et al. studied the phosphoric acid redistribution in hydrogen pumping mode within the membrane by using platinum micro electrodes embedded in the membrane.<sup>14</sup>

Furthermore, post mortem optical emission spectroscopy with inductively coupled argon plasma (ICP-OES) was utilized to study the redistribution within the MEA by Wannek et al.<sup>27</sup> Another common approach is to combine XTM imaging with pore network modeling (PNM). Chevalier et al.<sup>28</sup> combined synchrotron based XTM with PNM to investigate phosphoric acid redistribution within the gas diffusion electrode. Bevilacqua et al.<sup>29</sup> performed phosphoric acid injection experiments into gas diffusion layers and combined it with PNM, in order to investigate the influence of different types of gas diffusion layers and MPLs.

Both XTM and EIS are utilized in this work, but for the first time, they are performed simultaneously to directly correlate images and electrochemical properties and furthermore, other than in previous works, the XTM parameters were chosen as such to enable imaging of phosphoric acid not only in the GDL, but analyze also the microporous and catalyst layers.

In order to flood the anode GDL, phosphoric acid has to be transported from the membrane through the catalyst and the microporous layers. The pore sizes of these layers are too small to be resolved with operando XTM, however, both of these layers contain cracks with widths up to 150  $\mu\text{m}$ . Phosphoric acid saturation and redistribution in these cracks is analyzed and presented in this work. This allows examining the entire phosphoric acid pathway from the membrane to the flow field channel and also to determine the time constants for phosphoric acid flooding of all layers within this pathway.

Furthermore, imaging of phosphoric acid in the cracks of the catalyst layers allows studying the influence of phosphoric acid redistribution on the performance of HT-PEFCs in more depth. As previously described by Halter et al.,<sup>19</sup> an increase in current density triggers an increasing mass transport resistance as observed by EIS. However, this increase in mass transport resistance was not reflected in the overall cell voltage. It was speculated that this observation arises from the fact, that the mass transport losses are compensated by improved kinetics due to better wetting of phosphoric acid in either catalyst layer. Indirect imaging of changes of phosphoric acid in both catalyst layers is used to further elucidate this phenomenon.

\*Electrochemical Society Member.

<sup>z</sup>E-mail: [felix.buechi@psi.ch](mailto:felix.buechi@psi.ch)

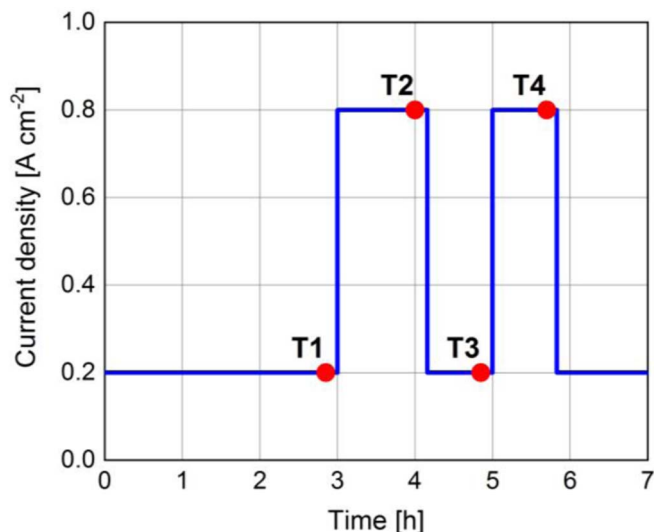


Figure 1. Current cycling experiment.

### Experimental

**General.**—All experiments were performed with materials from BASF for the membrane electrode assembly (MEA). A Celtec MEA consists of a PBI membrane doped with phosphoric acid with a thickness of 100  $\mu\text{m}$ . The electrodes consist of Vulcan XC-72 supported platinum catalyst with a Pt loading of 1  $\text{mg cm}^{-2}$  for both anode and cathode. This electrode was coated on a SGL 38 gas diffusion layer (GDL) including a microporous layer (MPL). The MEA was assembled and hot-pressed for 30 seconds at 140°C with a constant gap of 800  $\mu\text{m}$ . A specially designed HT-PEFC cell for XTM imaging with a circular active area of 20  $\text{mm}^2$  was used for all experiments.<sup>30</sup> In the cell-build reported here, the channels of the anode and cathode flow fields are slightly contorted i.e. not completely parallel to each other. MEA compression was limited by two 320  $\mu\text{m}$  PFA gaskets and a GDL compression of 20% was thus obtained.

A break-in procedure was carried out for 2 hours at a cell temperature of 160°C and at 0.2  $\text{A cm}^{-2}$  using 20  $\text{ml min}^{-1}$  of hydrogen at the anode and 20  $\text{ml min}^{-1}$  of oxygen at the cathode. The anode gas composition was then changed to 10%  $\text{H}_2$  in  $\text{N}_2$  with a constant total flow rate of 50  $\text{ml min}^{-1}$  and the break-in continued for 1 hour at 0.2  $\text{A cm}^{-2}$  for equilibration purposes. Both anode and cathode gases were humidified at room temperature. All experiments were then carried out with these gas compositions at anode and cathode. After the break-in, a current cycling protocol, as shown in Figure 1, was performed which involved two positive current steps (from 0.2  $\text{A cm}^{-2}$  to 0.8  $\text{A cm}^{-2}$ ) with a holding time of 70 min at 0.8  $\text{A cm}^{-2}$  for the first positive current step and 50 min for the second positive current step and a negative current step (from 0.8  $\text{A cm}^{-2}$  to 0.2  $\text{A cm}^{-2}$ ) in between with a holding time of 50 min at 0.2  $\text{A cm}^{-2}$ .

For the simultaneous EIS/imaging experiments, EIS Spectra were acquired 1 minute after the current step, then every 2 minutes by applying an AC voltage of 30 mV in the frequency range from 100 kHz to 100 mHz with 5 points per decade. Diluted hydrogen (10%  $\text{H}_2$  in  $\text{N}_2$ ) was used at the anode and pure oxygen at the cathode. This gas composition was chosen in order to observe mass transport limitations at the anode. A more detailed description of the EIS method and effects of the chosen gas composition on general performance was reported in Ref. 19.

The flooding of the catalyst layers (CL) and the microporous layers (MPL) was evaluated for the first positive current step between T1 and T2 by performing XTM scans every 2 minutes for the first 10 minutes after the positive current jump, every 5 minutes from minutes 10 to 20 after the current jump and then every 10 minutes for the remaining time of the current jump. Flooding of the anode GDL

was evaluated for the second positive current step, where additionally to XTM, Electrochemical impedance spectroscopy was measured as described above.

**XTM image acquisition.**—X-Ray tomographic imaging was carried out at the TOMCAT (Tomographic Microscopy and Coherent rAdiology experimenTs) beamline at the Swiss Light Source (SLS). Polychromatic radiation with a peak energy of about 30 keV was used for all experiments. The sample was placed about 10 mm from the (150  $\mu\text{m}$  thick LuAG:Ce) scintillator and for each tomographic scan, 2001 projections were acquired during 180° rotation with an exposure time of 11 ms each resulting in a total scan time of 22 s. The images were magnified by a 2–4x continuous zoom microscope system (Elysa Solutions). The magnification was set to 2.8x. A sCMOS camera (PCO.edge) with a chip size of 2560  $\times$  2160 pixels was used with a resulting voxel size of 2.3  $\mu\text{m}$  for all tomograms, which were reconstructed using a Fourier based algorithm.<sup>31,32</sup> Dark- and flatfield corrections were used for all tomographic scans.

**XTM image processing.**—Two different image processing pathways were used: i) segmentation and/or thresholding to determine the phosphoric acid content in the GDL and in the cracks of MPL and catalyst layer and ii) average gray scale value (GSV) evaluation for determination of the acid content in the catalyst layers.

For the segmentation/thresholding pathway, image processing was performed with a combination of Fiji (freeware), MATLAB and 3D Slicer (freeware). The reconstructed images were divided into GDL, MPL and CL for anode and cathode each. To gain information about the redistribution of phosphoric acid, the scans were aligned to the reference scan (at time T1) prior to the first positive current jump using 3D Slicer. The reference scan at T1 was then subtracted from the later scans and these differential images were further filtered by applying a median (3D, 3px) and an anisotropic diffusion filter using MATLAB. After filtering, the subtracted scans were segmented into the void and phosphoric acid phases by thresholding. The segmented data were treated with a 3D clearing filter using MATLAB.

This procedure allows for quantifying the changes in phosphoric acid redistribution in consecutive scans. For the segmentation of the reference scan at T1 into carbon and void phases, the same filtering and segmentation pipeline was used for the GDL part as described above. The segmentation of the cracks in the microporous and the catalyst layers was done manually.

A region of interest of 1209  $\times$  1632 pixels (2781  $\times$  3754  $\mu\text{m}$ ) was chosen to study the redistribution of phosphoric acid in the GDL; for the analysis of the phosphoric acid redistribution within the cracks of the MPL and CL, a region of interest of 1077  $\times$  1077 pixels (2477  $\times$  2477  $\mu\text{m}$ ) was chosen.

For the mean GSV evaluation of the acid content and acid concentration changes in the catalyst layers, an initial volumetric composition of the catalyst layer was assumed to be as follows: 50 vol. % empty pore volume, 20 vol. % initial phosphoric acid content with an initial concentration of 100 wt. %, 0.1 vol. % platinum and 29.9 vol. % carbon. With a voxel edge length of 2.3  $\mu\text{m}$ , this volumetric composition creates a sub-voxel composition of layers of each materials with layer thickness of 1.15  $\mu\text{m}$  for void, 0.46  $\mu\text{m}$  for phosphoric acid, 0.002  $\mu\text{m}$  for platinum and 0.688  $\mu\text{m}$  for carbon.

In order to compare the mean GSV in the catalyst layers between scans at different time steps, one representative slice in the middle of the CL was chosen. To compensate for small overall GSV variations in consecutive scans, the mean GSV in the CL slice was compared to the mean GSV of a slice in the cathode flow field as a reference. The cathode flow field was chosen as reference, because phosphoric acid, which is the only mobile phase, was never observed in the cathode flow field during the entire current cycling experiment.

The linear attenuation coefficients for the polychromatic radiation used were approximated with the linear attenuation coefficients at 30 keV for each material. The linear attenuation coefficients of 100 wt. % phosphoric acid was set to 1.02  $\text{cm}^{-1}$ ,<sup>33</sup> the one of water to 0.14  $\text{cm}^{-1}$ <sup>33</sup> and of the void to 0  $\text{cm}^{-1}$ . The volume of the platinum

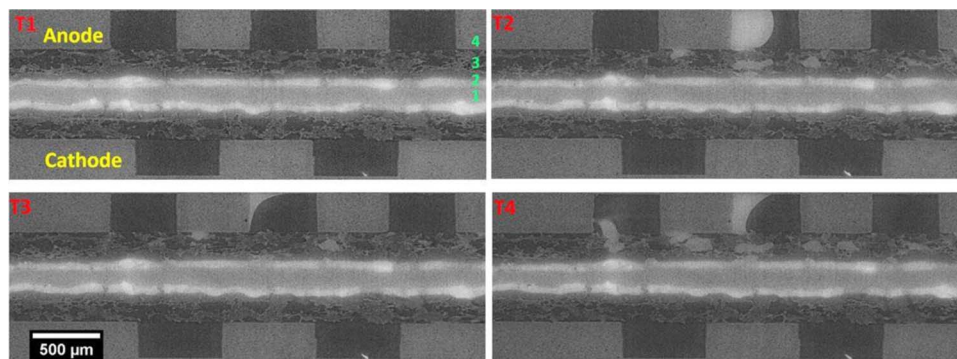


**Figure 2.** Vertical slices from the tomographic scans at times T1 to T4 (as denoted in Figure 1), showing the flow fields (4), GDL/MPL (3), catalyst layers (2) for the anode on top and the cathode on the bottom with the membrane in the middle (1) (white: catalyst layers; bright grey: phosphoric acid, light grey: carbon fibers, dark grey: pore space and flow field channels).

and carbon phases were assumed to be constant. At time T1, the attenuation of a voxel of the catalyst layer, which can be considered as its gray scale value (GSV) can be described as follows:

$$GSV^1 \approx -\ln\left(\frac{I^1}{I_0^1}\right) \approx \mu_{Pt} * x_{Pt}^1 + \mu_C * x_C^1 + \mu_{PA}^1 * x_{PA}^1 + \mu_{air} * x_{air}^1 \quad [1]$$

where  $I^1$  is measured intensity,  $I_0^1$  is the intensity measured without sample,  $\mu^1$  is the linear attenuation coefficient and  $x^1$  is the layer thickness in the sub-voxel volume for each material at time T1. This correlation also holds for later time steps (i.e. T2).

$$GSV^2 \approx -\ln\left(\frac{I^2}{I_0^2}\right) \approx \mu_{Pt} * x_{Pt}^2 + \mu_C * x_C^2 + \mu_{PA}^2 * x_{PA}^2 + \mu_{air} * x_{air}^2 \quad [2]$$

The difference in GSV between the two scans can be described as follows:

$$\Delta GSV = \mu_{Pt} * (x_{Pt}^2 - x_{Pt}^1) + \mu_C * (x_C^2 - x_C^1) + \mu_{PA}^2 * x_{PA}^2 - \mu_{PA}^1 * x_{PA}^1 + \mu_{air} * (x_{air}^2 - x_{air}^1) \quad [3]$$

When assuming no changes in the contribution of platinum and carbon and by setting the attenuation coefficient of the void to 0 (s. Equation 4), the difference in GSV between two scans only depends on the volumetric fraction and the attenuation coefficient of phosphoric acid (s. Equation 5). The same argumentation can be made for the mean GSV (mGSV) of a slice in a CL for scans at different time steps. For this analysis, a region of interest of  $1077 \times 1077$  pixels ( $2477 \times 2477 \mu m$ ) was chosen.

$$\text{With } x_{Pt}^2 - x_{Pt}^1 = x_C^2 - x_C^1 = \mu_{air} = 0 \text{ follows,} \quad [4]$$

$$GSV^2 - GSV^1 = \mu_{PA}^2 * x_{PA}^2 - \mu_{PA}^1 * x_{PA}^1 \quad [5]$$

## Results

This section describes the results of the phosphoric acid redistribution in the MEA triggered by a positive current step. First, the phosphoric acid redistribution will be discussed separately for the invasion of the pores of the GDL, the cracks of the microporous and for the acid movement in the catalyst layers. Later, the influence of the phosphoric acid redistribution within these layers on the performance of a HT-PEFC will be analyzed.

**Gas diffusion layer flooding and mass transport effects.**—As shown in Figure 1, two positive current steps were performed of which the first was held for 70 minutes and the second for 50 minutes, with a negative current step of also 50 minutes in between. Figure 2 shows a vertical XTM slices for the scans T1 to T4 (times as indicated in Figure 1).

After completion of the break-in at T1, it can be observed, that no phosphoric acid is found in either GDL. At the end of the first current step, the anode GDL and the flow field channel are flooded with phosphoric acid (T2). During the 50 min at low current density, the phosphoric acid content in the anode GDL and flow field channel is reduced (T3). The second positive current step causes again an increase of phosphoric acid flooding of both, the anode GDL and the flow field channels (T4). During the entire current density sequence no changes in the cathode GDL or flow field channels, respectively, were observed. The positive current step therefore triggers phosphoric acid movement toward the anode, while after decreasing the current density, the phosphoric acid amount in the anode GDL and flow field channel is reduced but not fully emptied.

These observations are well in line with the results of Eberhardt et al.<sup>12</sup> who investigated a similar current step protocol and observed the same correlation between current density and phosphoric acid content in the anode GDL and flow field channels.

When quantifying the additional amount of phosphoric acid in the anode GDL over time for the second flooding step (from T3 to T4) obtained from operando XTM, a steep, initial increase in PA content of the anode GDL is observed for the first 20 minutes, after which, the increase starts to level off at about  $80 \text{ mm}^3 \text{ cm}^{-2}$  (see Figure 4), which is similar to the values observed by Eberhardt et al. in the same time range.

It has previously been shown that when using diluted hydrogen simulating reformat conditions, an increase of mass transport resistance can be observed by EIS after a positive current steps,<sup>19</sup> hypothesized to be caused by acid saturation in the anode GDL. However this correlation could not be verified directly without simultaneous imaging. In order to substantiate this correlation of phosphoric acid flooding of the GDL and the mass transport effect at the anode, simultaneously to the XTM imaging, electrochemical impedance spectra were measured. The measured EIS spectra are shown in Figure 3.

Only in the low frequency region (LFR) changes are observed, which can be correlated to increasing mass transport resistances under the chosen operating conditions (10%  $\text{H}_2$  in  $\text{N}_2$ ). The occurring changes in the LFR are normalized (1 min = 0%; 45 min = 100%) and are plotted in Figure 4. Previous data from a differential  $2 \text{ cm}^2$  cell, where the LFR was measured with higher temporal resolution (for experimental details see)<sup>19</sup> are shown for comparison together with the normalized EIS data from the  $0.2 \text{ cm}^2$  XTM cell as well as phosphoric acid changes in the anode GDL on an absolute and normalized scale.

As seen in Figure 4, for the LFR responses and the PA content of the GDL, a similar temporal behavior is observed. In order to quantify the temporal evolution, a time constant was fitted using the following function:

$$f(x) = a * \exp\left(\frac{-t}{b}\right) + c \quad [6]$$

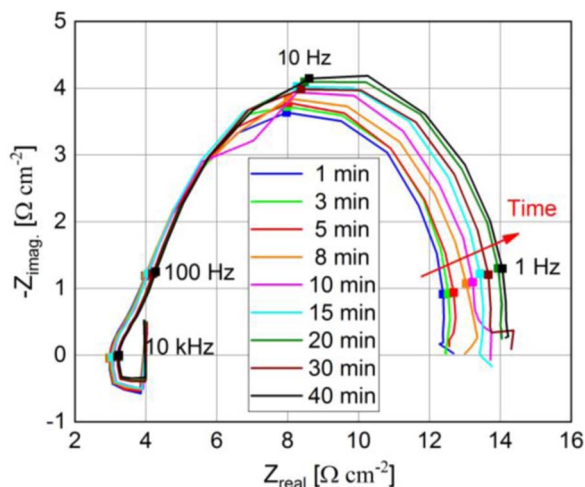


**Figure 3.** Consecutive EIS measurements after a positive current step at times indicated at 160°C for a cell operated with diluted hydrogen.

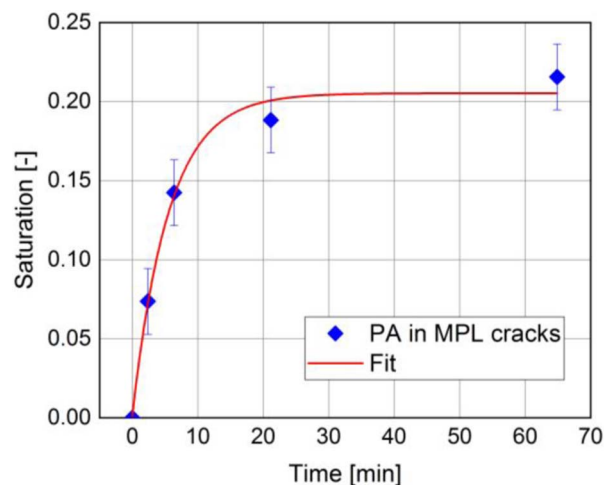


**Figure 6.** Phosphoric acid flooding of the anode MPL cracks after a current step from 0.2 to 0.8 A cm<sup>-2</sup> at 160°C.

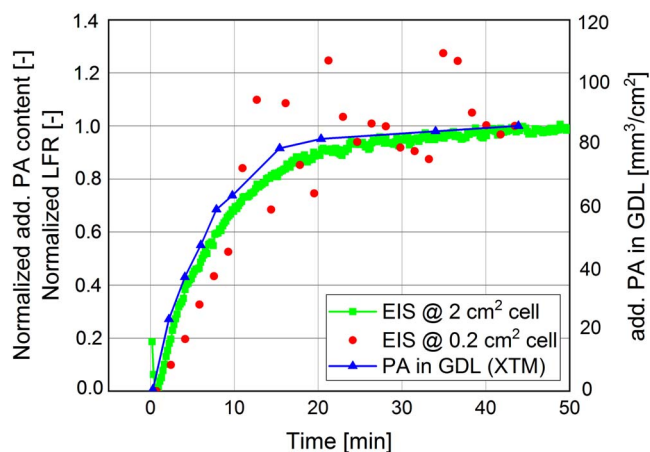


**Figure 4.** Blue points: temporal evolution of the additional phosphoric acid amount in the anode GDL after a positive current jump (T3 to T4) as absolute (right scale) and normalized (left scale) values; red points: normalized real part of the EIS 1 Hz response of the 0.2 cm<sup>2</sup> imaging cell (20 mm<sup>2</sup> active area) and green points: normalized 1 Hz signal of 2 cm<sup>2</sup> cell.

where  $t$  is the time,  $a$  and  $c$  are fitting parameters and  $b$  is the time constant, which was determined for all normalized data sets. All time constants were found to be between 7 and 8 minutes, therefore showing a good agreement between EIS measurements and the flooding of the anode GDL. This shows that the described EIS method can be used to monitor the phosphoric acid flooding of the anode GDL after a positive

current step. That is, for diluted hydrogen operation phosphoric acid saturation of the anode GDL can indeed be monitored by analysis of the LFR.

**Flooding of the anode MPL cracks.**—In order to flood the anode GDL, phosphoric acid has to be transported from the membrane through the catalyst and MPL layers. The microporous layer acts as an obstacle in this path, as the pores of the MPL are difficult to invade due to their small pore size below 1 μm<sup>34</sup> and the non-wetting nature of the phosphoric acid on PTFE. However, the MPL contains both elongated cracks and round uncoated areas (holes). Both features will be referred to from here on as cracks. These cracks have widths of up to 150 μm, which can be invaded at lower capillary pressures. The flooding of the MPL cracks seems to be a relatively fast process, as flooding of the first MPL cracks is observed already 2 minutes after a positive current step (see Figure 5 left). These cracks serve as a gateway for phosphoric acid to penetrate the MPL and therefore do not hinder the flooding of the anode GDL and are filled further with time.

The temporal behavior of the PA saturation in the cracks is shown in Figure 6. An increase in saturation (in 2D) is observed for the first 20 minutes then the saturation levels off and only minor changes can be observed for the remaining 45 minutes, with the saturation stabilizing at  $22 \pm 2\%$  (s. Figure 5 right). During this time, the filling of both, large and small cracks is observed. The error bars were determined by a threshold variation in the segmentation of  $\pm 2\%$ .

The time constant for the flooding of the MPL cracks was determined by using Equation 6 as a fitting function and determined to be  $5.5 \pm 1.0$  min.

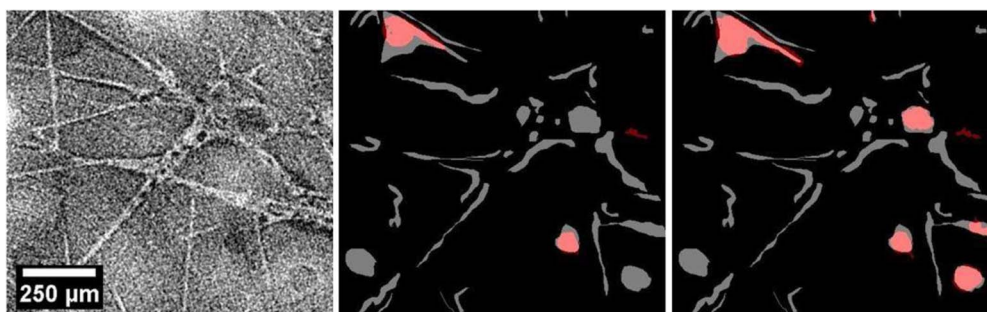


**Figure 5.** Horizontal XTM-slices of the MPL; left: GSV image of the interface MPL/GDL at time T1; middle: 2 min after current step from 0.2 to 0.8 A cm<sup>-2</sup>; right: after 65 min; grey: anode MPL cracks; red: phosphoric acid in MPL cracks.

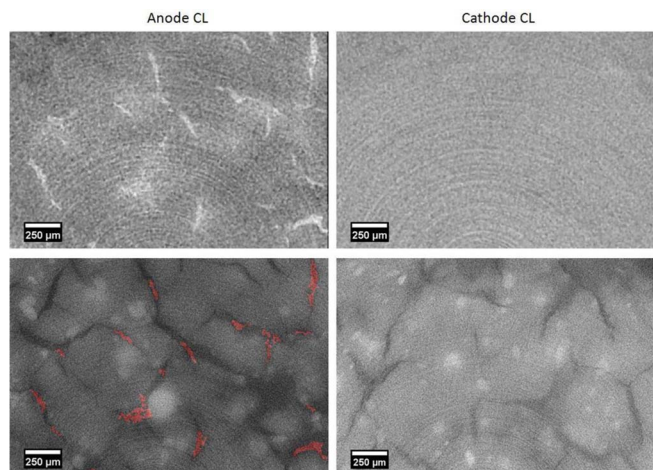


**Figure 7.** Horizontal XTM-slices of the (left) anode and (right) cathode catalyst layers; top row: differential image of the CL between T1 and T2; bottom row: GSV image of the CL overlaid with the segmented phosphoric acid (red) from the differential image.

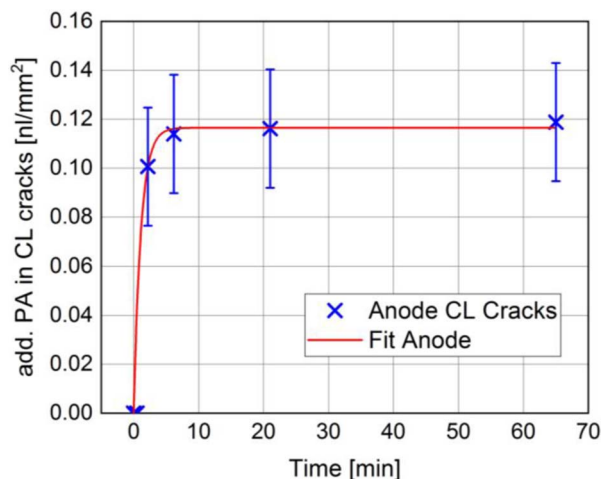


**Figure 8.** Additional phosphoric acid content of the anode CL cracks after a positive current step.

**Flooding of the catalyst layers.**—The catalyst layer consists mainly of carbon supported platinum, phosphoric acid and void. The pores in the catalyst layer have a pore size below 1  $\mu\text{m}$ ,<sup>35,36</sup> which cannot be resolved with the current operando XTM voxel size. However, similar to the microporous layer described above, the catalyst layer also contains large cracks of up to 150  $\mu\text{m}$  width and current XTM settings with a voxel edge length of 2.3  $\mu\text{m}$  can be used to gain information about the phosphoric acid content in these cracks. The contrast of phosphoric acid and void is highly reduced inside these cracks due to the strong X-ray absorption of platinum, therefore, the initial state of phosphoric acid cannot be determined; however additional PA may be observed.

With the image subtraction workflow (see Experimental), the changes of the phosphoric acid content in both anode and cathode catalyst layer cracks can be determined. Figure 7 shows a slice of the differential image between the scans T1 and T2 for both the anode and the cathode catalyst layers (top) and the segmented changes of phosphoric acid content (bottom).

In the cathode catalyst layer cracks no changes of the PA content were observed during the entire cycling protocol while in the anode catalyst layer a significant increase in the phosphoric acid content in the cracks can be observed after positive current jumps.

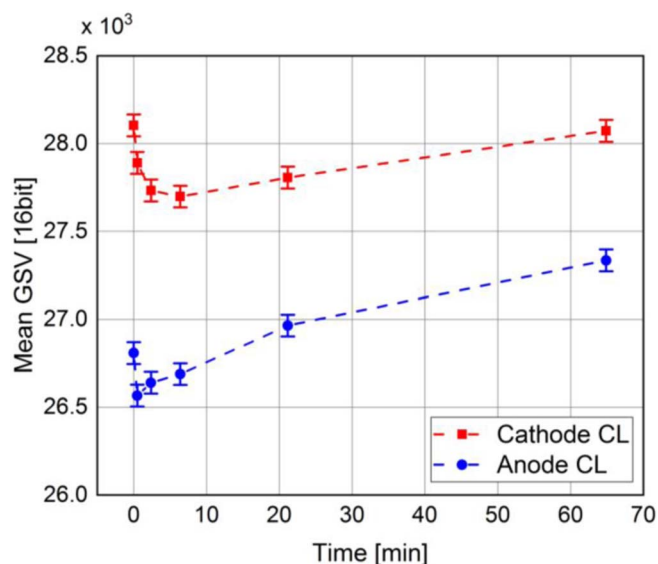


**Figure 9.** Mean GSV of a slice in the center of the anode CL (blue) and the cathode CL (red); error bars were determined by the standard deviation of the GSV in the anode CL slice at time T1.

Figure 8, shows the additional amount of phosphoric acid in the anode CL cracks over time.

Already 2 minutes after the current step, the anode CL cracks show a significant increase in phosphoric acid content. A time constant of  $0.9 \pm 0.1$  min can be determined using Equation 6. This fast flooding of the anode CL cracks seems reasonable, on the one hand being close to the membrane bulk and on the other hand requiring low capillary pressure due to their large width. The fact that 2 minutes after the current step, phosphoric acid is also found in MPL cracks and to a small amount in the anode GDL supports the presence of phosphoric acid in the catalyst layer cracks. This is required in order to establish a continuous pathway from the membrane to the GDL.

However, when considering a very short interval of only 30 s after the current step the anode CL cracks show no changes. The mechanistic reason for this “delay” is unclear, but a phenomenon with a similar time delay was observed in EIS measurement in the 2  $\text{cm}^2$  cell, where EIS was measured with a time resolution of 10 s. For the first 30 seconds, a drop in the low frequency resistance was observed (see first green point in Figure 4). Both observations indicate that there is a counterforce to phosphoric acid migration, which is dominating during the first 30 seconds after the current increase. A possible explanation for this phenomenon is the following: due to the required capillary pressure for the flooding of the cracks in the catalyst layer, the phosphoric acid content at the anode side of the membrane is increased before the catalyst layer cracks are flooded, as acid pressure has to build up first.

In the anode catalyst layer, obviously, the acid filling of the cracks is current density dependent, which is relevant for the acid migration to the MPL and GDL. However this does not give any information about the acid wetting of the catalyst layer itself. As stated above, the pore structure of the catalyst layers cannot be resolved with the current XTM set-up with a voxel size of 2.3  $\mu\text{m}$ . But, also without resolving the porous structure, information about the changes of phosphoric acid content in the CL bulk can be derived by analyzing the changes of the mean grayscale value (mGSV) in the catalyst layer after a current density step. To do so, a normalization of the mGSV was carried out, using the mean GSV of the cathode flow field as a reference (details see experimental section).

The changes in normalized mGSV of a slice in the center of the anode and cathode catalyst layers as function of time after the current step are shown in Figure 9. In the anode CL, a drop is observed during the first 30 seconds, followed by a steady increase during the high

current step. In the cathode CL, a drop in mGSV is observed during the first 6 minutes, again followed by an increase for the remainder of the high current step. The error bars in Figure 9 are given by the standard deviation of the GSV in the anode CL slice at time T1.

The changes in GSV in the bulk phase of the catalyst layers can be attributed to phosphoric acid, as it is the only mobile phase. Changes can be either due to a change in the amount of phosphoric acid in the catalyst layer or due to changes in its concentration. The differentiation of the two effects is not trivial; however, the following hypothesis can be made.

The changes in GSV in the cathode CL are attributed to the changes in phosphoric acid concentration. This is due to the fact, that after a positive current step, more water is produced at the cathode and therefore, a dilution of phosphoric acid can be expected. Also, no significant changes in the phosphoric acid saturation in the cracks of the cathode CL were observed; therefore acid movement from the cracks into the membrane or smaller pores of the catalyst layer bulk seems unlikely.

The changes in GSV in the anode CL are attributed to changes in phosphoric acid saturation. Even though the increased water transport through the membrane after the current jump may affect the GSV, the changing GSV in the anode catalyst layer is likely dominated by the increasing phosphoric acid content. The increased water production at the cathode is therefore assumed to not affect the phosphoric acid concentration at the anode. As at the same time, flooding of the anode CL cracks is observed. An increase in saturation of the bulk catalyst layer pores seems the most likely cause for an increasing GSV.

Based on these arguments, the mGSV changes in the cathode CL are assumed to be changes in phosphoric acid concentration and mGSV changes in the anode CL are assumed to be due to changes of phosphoric acid saturation. In order to estimate the change of saturation of phosphoric acid in the anode and the dilution at the cathode CL the following assumptions are made:

All changes on the anode are attributed to saturation changes of the CL pore space, assuming a constant acid concentration of 100 wt. %, which attributes then the mGSV changes to changes of the acid volume fraction only:

$$GSV^2 - GSV^1 = \mu_{PA} * (x_{PA}^2 - x_{PA}^1) \quad [7]$$

where  $\mu_{PA}$  is the linear attenuation coefficient for phosphoric acid with a concentration of 100 wt. % and  $x_{PA}$  are the sub-voxel layer thicknesses of phosphoric acid at different times. The derivation for Equations 7 and 8 has been given in the experimental section.

At the cathode, all changes are attributed to the acid concentration at constant volume fraction. The changes in GSV at the cathode are interpreted as changes of the linear attenuation coefficient due to the changing ratio of the phosphoric acid/water mixture:

$$GSV^2 - GSV^1 = (\mu_{PA}^2 - \mu_{PA}^1) * x_{PA} \quad [8]$$

where the symbols have the same meanings as described for Equation 7.

As changes in attenuation coefficient in Eq. 8 are based on vol. %, in order to express the changes in wt. %, the ratio of the molar weights and densities of water and phosphoric acid have to be factored in.

Phosphoric acid volume fraction and concentration changes in the anode and cathode catalyst layers are shown in Figure 10. In the anode CL an initial drop of the phosphoric acid content of about 1 vol. % in the first 30 seconds is observed. Afterwards the phosphoric acid content increases to a total content of 22.3 vol. % after 65 minutes, a relative increase of about 15%. The equilibrium state was not yet reached 1 hour after the positive current step. The lines in Figure 10 are time constant fits according to Equation 6, for the flooding of the anode catalyst layer a time constant of  $39 \pm 7$  minutes is determined.

In the cathode CL, phosphoric acid shows a dilution for the first 6 minutes where it reaches a minimum concentration of 99 wt. %. After that, the concentration increases again and reaches the initial concentration of 100 wt. % after 65 minutes. This increase may be related to phosphoric acid condensation and the time required to establish an equilibrium state after a current jump, as condensed species,

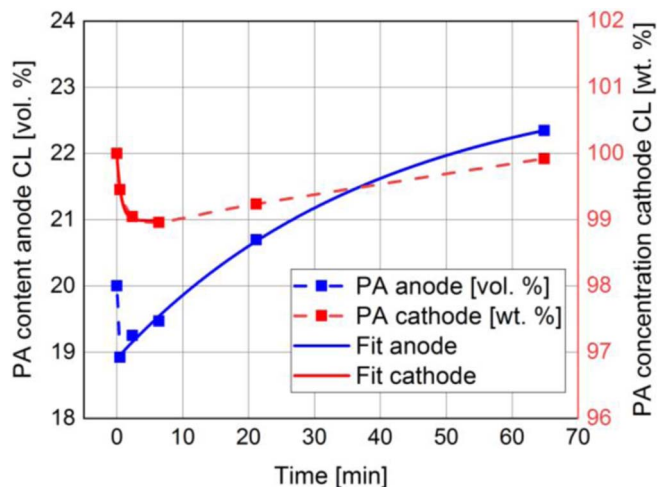


**Figure 10.** Phosphoric acid flooding of the anode catalyst layer (blue); Phosphoric acid concentration in the cathode CL (red).

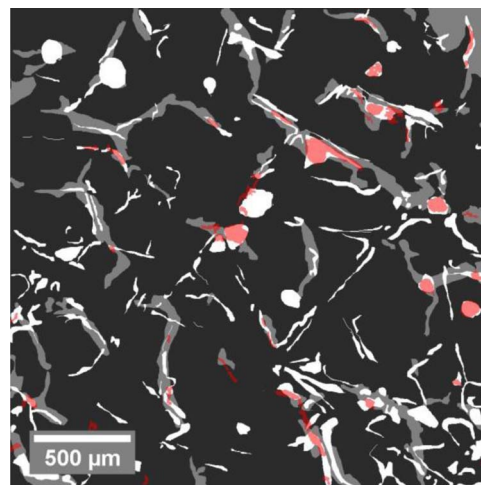


**Figure 11.** Combined horizontal XTM-slices of the anode CL cracks (gray) and the anode MPL cracks (white) combined with phosphoric acid content in the MPL cracks 65 minutes after the current step (red).

such as  $H_4P_2O_5$ , alter the attenuation coefficient of phosphoric acid. For the phosphoric acid dilution in the cathode catalyst layer, a time constant of  $0.7 \pm 0.1$  minutes is determined. It should be noted, that the obtained time constants are independent of the assumption on the catalyst layer composition, which is only affecting the extent of these changes, but not their temporal behavior.

**The path of phosphoric acid.**—In the sections above, the phosphoric acid flooding of the anode as a response to a current step from  $0.2$  to  $0.8 \text{ A cm}^{-2}$  at  $160^\circ\text{C}$  was discussed for the catalyst layer, the MPL and the GDL separately. However, in order to flood the anode flow field channel, where phosphoric acid loss is occurring, a phosphoric acid pathway from the membrane to the flow field channel has to be established. In this path, phosphoric acid has to penetrate all three layers, as discussed above. The goal of this section is to discuss the interplay of these layers and their role in the determination of the established phosphoric acid path.

Figure 11 shows an overlay of the anode catalyst layer cracks (gray), the MPL cracks (white) and phosphoric acid found in the MPL cracks 65 minutes after the current step (red). It is seen that MPL cracks often overlap with the cracks in the catalyst layer, meaning that MPL cracks are often found above CL cracks, thereby creating a pathway for phosphoric acid from the membrane to the GDL.

**Table I.** Time constants for phosphoric acid flooding in the different layers of the anode and phosphoric acid dilution in the cathode CL as determined using Equation 6.

PA flooding in	Time const. [min]
anode CL	$39 \pm 7$
cathode CL (dilution)	$0.7 \pm 0.1$
anode CL cracks	$0.9 \pm 0.1$
anode MPL cracks	$5.6 \pm 0.9$
anode GDL	$6.8 \pm 0.3$

Furthermore, it can be observed that only those MPL cracks are invaded by phosphoric acid which have a connection to a CL crack. It therefore becomes obvious that it is not the cracks in the MPL that determine the paths of the phosphoric acid, but rather the cracks in the CL, as they act as a gateway for PA transport from the membrane to the MPL. Therefore, only MPL cracks above these gateways are invaded by phosphoric acid and only after crossing collocated MPL cracks phosphoric acid penetrates into the GDL and eventually reaches out to the flow field channel. By this process, continuous pathways from the membrane to the anode flow field are established and the location of these pathways is dominated by the CL cracks.

This mechanistic view of acid transport is supported by the time constants of the acid saturation changes in the different layers. Table I shows a summary of the time constants for the phosphoric acid flooding of all involved layers. The changes in saturation are fastest in the catalyst layers (except for anode CL bulk), followed by the MPL cracks and finally for the saturation of the GDL.

**The influence of phosphoric acid redistribution on cell performance.**—The EIS measurement in Figure 4 shows an increase in the LFR, indicating an increasing mass transport resistance due to the flooding of the anode GDL when the cell is operated with diluted hydrogen, i.e. under simulated reformat conditions. Despite the similar time constants for the phosphoric acid flooding in the anode GDL determined by operando XTM and EIS measurements, the observed increasing mass transport resistances might not arise only from GDL flooding. The first EIS measurement was completed 1 min after the current jump, when flooding of the anode catalyst layer cracks already started to occur (time constant = 0.9 minutes). Therefore, the first EIS measurement which was used as reference already includes some mass transport losses due to flooding of CL cracks, as already significant changes in the catalyst layer have occurred. However, flooding of the MPL cracks and GDL pores with time constants between 5 and 8 minutes is slower, which is then reflected in the EIS measurements. Therefore, mainly mass transport losses due to GDL and MPL cracks flooding are captured by EIS.

Figure 12 shows the cell voltage as function of time after a positive current step. Two trends can be observed. For the first 2 minutes, a strong increase in cell voltage is observed, which correlates well with the time domain for the changes of acid saturation in the anode catalyst layer cracks and the acid dilution in the cathode CL. This indicates that one or both of these processes lead to an improvement in cell voltage due to an improved wetting of the catalyst layer with phosphoric acid; thereby improving the kinetics. After 2 minutes, the cell voltage peaks and then drops during the next ca. 20 minutes, before leveling off. This drop in cell voltage is in the same time range as is observed for the GDL and MPL crack flooding. The observed voltage decrease can therefore be correlated with an increasing of mass transport resistance due to the migration of the acid into MPL cracks and the GDL. These mass transport losses are observed within the EIS measurement.

The influence of PA redistribution after a positive current step is therefore twofold: the changes of acid saturation in the anode catalyst layer and eventually those in acid concentration on the cathode side improve the cell voltage during the first 2 minutes by improving the kinetics, after which mass transport losses are occurring due to increased GDL and MPL PA saturation, which reduces the cell voltage

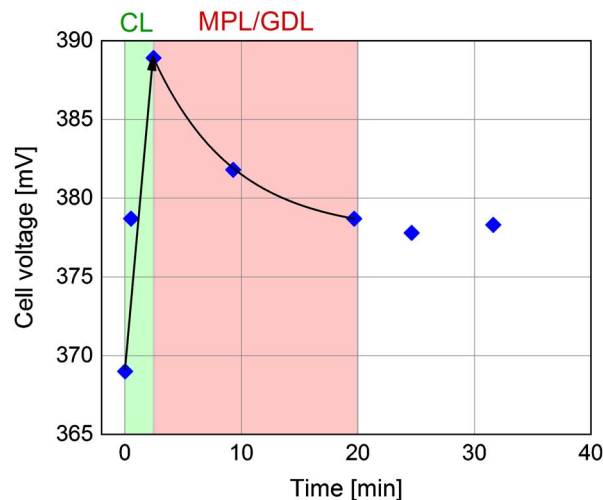


**Figure 12.** Impact of phosphoric acid redistribution on the cell voltage; Green: Cell voltage increase due to anode CL cracks flooding and phosphoric acid dilution in the cathode CL; Red: Cell voltage decrease due to flooding of the MPL and GDL.

for the next 20 minutes before cell performance reaches a new steady state.

## Conclusions

Synchrotron based, operando X-ray tomographic microscopy was used to study the redistribution of phosphoric acid within a HT-PEFC MEA triggered by a positive current step. After the current density increase, flooding of the cracks in the anode catalyst layer, the anode MPL and the macro-pores of the anode GDL are observed. The cathode does not show any changes in its phosphoric acid content in either of these layers.

In the anode catalyst layer, the cracks get flooded with a time constant of about 1 minute. The cracks of the catalyst layer and the MPL are often positioned on top of each other (mainly related to the consecutive coating process of both layers). Only MPL cracks that overlap with those in the catalyst layer get invaded with phosphoric acid. It is therefore the catalyst layer cracks that are defining the location of the pathway of phosphoric acid from the membrane to the GDL. A change in the normalized GSV over time of the catalyst layers bulk material was found for both the cathode and the anode. This was interpreted as follows: at the cathode, the increased water production leads to a dilution of phosphoric acid with a time constant of 0.7 minutes. At the anode, phosphoric acid is invading the catalyst layer pore structure with a time constant of 39 minutes.

Similar to the catalyst layers, the MPL has cracks with a width of up to 150  $\mu\text{m}$ . These cracks get flooded with phosphoric acid with a time constant of 5.5 minutes and equilibrate with a saturation of around 20%.

After penetration of the cracks in the anode CL and MPL, flooding of the anode GDL starts after about 2 minutes and equilibrates after 20 minutes with a time constant of 7 minutes. The flooding of the anode GDL results in an increasing mass transport resistance, which was measured by evaluating the low frequency resistance of the electrochemical impedance spectroscopy measurement. The change of the transport resistance has a similar time constant as the MPL crack and GDL flooding.

The effects of the described redistribution of phosphoric acid on the performance of the cell, operated under reformat conditions, i.e. diluted hydrogen, are twofold. During the first two minutes, an increase in the cell voltage is observed which is expected to be due to the better wetting in the anode CL cracks, which is improving the kinetics as well as the dilution of phosphoric acid in the cathode CL. From 2 minutes to 20 minutes, the cell voltage drops due to



the increasing mass transport resistance induced by the flooding of the GDL and the MPL cracks. After 20 minutes, the cell voltage equilibrates, which is in line with the GDL/MPL cracks flooding time constants.

As acid migration into the anode GDL and gas channel is considered a degradation mechanism, the elucidation of the acid migration pathways paves the way for mitigation of this process. Future work will explore mitigation strategies, i.e. by tailoring crack density in the catalyst and MPL layers.

### Acknowledgment

The authors thank T. Gloor for software and test bench support; H. Xu, A. Mularczyk, M. Bühner, T. Schuler and J. Eller for their support at the TOMCAT beamline. All MEA materials were provided by BASF SE, which is gratefully acknowledged.

### ORCID

T. J. Schmidt  <https://orcid.org/0000-0002-1636-367X>  
F. N. Büchi  <https://orcid.org/0000-0002-3541-4591>

### References

1. S. Simon, F. Zhou, V. Liso, S. Lennart, J. Rabjerg, S. Thomas, X. Gao, S. S. Araya, F. Zhou, V. Liso, S. L. Sahlin, J. R. Vang, S. Thomas, X. Gao, C. Jeppesen, and S. K. Kær, "A comprehensive review of PBI-based high temperature PEM fuel cells," *Int. J. Hydrogen Energy*, **1**, 1 (2016).
2. S. Yu, L. Xiao, and B. C. Benicewicz, "Durability Studies of PBI-based High Temperature PEMFCs," *Fuel Cells*, **8**, 165 (2008).
3. J. Mader, L. Xiao, T. J. Schmidt, and B. C. Benicewicz, "Polybenzimidazole/acid complexes as high-temperature membranes," in: G. G. Scherer, (Ed.), *Adv. Polym. Sci. Cells II*, Springer, Berlin Heidelberg, 2008: pp. 63.
4. G. Neophytides and T. J. Schmidt, "High-Temperature Polymer Electrolyte Fuel Cells," in: *Encycl. Appl. Electrochem.*, 2014: pp. 996.
5. D. W. Shin, M. D. Guiver, and Y. M. Lee, "Hydrocarbon-Based Polymer Electrolyte Membranes: Importance of Morphology on Ion Transport and Membrane Stability," *Chem. Rev.*, **117**, 4759 (2017).
6. R. Zeis, "Materials and characterization techniques for high-temperature polymer electrolyte membrane fuel cells," *Beilstein J. Nanotechnol.*, (2015).
7. F. Conti, A. Majerus, D. Noto, and C. Korte, "Raman study of the polybenzimidazole – phosphoric acid interactions in membranes for fuel cells," *Phys. Chem. Chem. Phys.*, **14**, 10022 (2012).
8. K. A. Perry, K. L. More, E. A. Payzant, R. A. Meisner, B. G. Sumpter, and B. C. Benicewicz, "A Comparative Study of Phosphoric Acid-Doped m-PBI Membranes," *J. Polym. Sci. Part B Polym. Phys.*, **52**, 26 (2014).
9. Q. Li, R. He, R. W. Berg, H. A. Hjuler, and N. J. Bjerrum, "Water uptake and acid doping of polybenzimidazoles as electrolyte membranes for fuel cells," *Solid State Ionics*, **168**, 177 (2004).
10. F. Mack, S. Heissler, R. Laukenmann, and R. Zeis, "Phosphoric acid distribution and its impact on the performance of polybenzimidazole membranes," *J. Power Sources*, **270**, 627 (2014).
11. S. H. Eberhardt, F. Marone, M. Stampanoni, F. N. Büchi, and T. J. Schmidt, "Operando X-ray Tomographic Microscopy Imaging of HT-PEFC: A Comparative Study of Phosphoric Acid Electrolyte Migration," *J. Electrochem. Soc.*, **163**, F842 (2016).
12. S. H. Eberhardt, M. Toulec, F. Marone, M. Stampanoni, F. N. Büchi, and T. J. Schmidt, "Dynamic Operation of HT-PEFC: In-Operando Imaging of Phosphoric Acid Profiles and (Re)distribution," *J. Electrochem. Soc.*, **162**, F310 (2015).
13. H. Becker, U. Reimer, D. Aili, L. N. Cleemann, J. O. Jensen, W. Lehnert, and Q. Li, "Determination of Anion transference Number and Phosphoric Acid Diffusion Coefficient in High Temperature Polymer Electrolyte Membranes," *J. Electrochem. Soc.*, **165**, F863 (2018).
14. H. Becker, L. N. Cleemann, D. Aili, J. O. Jensen, and Q. Li, "Probing phosphoric acid redistribution and anion migration in polybenzimidazole membranes," *Electrochem. Commun.*, **82**, 21 (2017).
15. D. Henkensmeier, N. M. H. Duong, M. Brela, K. Dyduch, A. Michalak, K. Jankova, H. Cho, J. H. Jang, H. J. Kim, L. N. Cleemann, Q. Li, and J. O. Jensen, "Tetrazole substituted polymers for high temperature polymer electrolyte fuel cells," *J. Mat. Chem. A*, **3**, 14389 (2015).
16. J. Eller, J. Roth, F. Marone, M. Stampanoni, and F. N. Büchi, "Operando Properties of Gas Diffusion Layers: Saturation and Liquid Permeability," *J. Electrochem. Soc.*, **164**, F115 (2017).
17. I. V. Zenyuk, D. Y. Parkinson, G. Hwang, and A. Z. Weber, "Probing water distribution in compressed fuel-cell gas-diffusion layers using X-ray computed tomography," *Electrochem. Commun.*, **53**, 24 (2015).
18. M. F. Mathias, J. Roth, J. Fleming, and W. Lehnert, "Diffusion media materials and characterisation," in: *Handb. Fuel Cells – Fundam. Technol. Appl.*, 2010.
19. J. Halter, S. Thomas, S. K. Kær, T. J. Schmidt, and F. N. Büchi, "The Influence of Phosphoric Acid Migration on the Performance of High Temperature Polymer Electrolyte Fuel Cells," *J. Power Sources*, **399**, 151 (2018).
20. W. Maier, T. Arlt, K. Wippermann, C. Wannek, I. Manke, W. Lehnert, and D. Stolten, "Investigation of HT-PEFCs by Means of Synchrotron X-ray Radiography and Electrochemical Impedance Spectroscopy," *ECS Trans.*, **41**, 1413 (2011).
21. W. Maier, T. Arlt, C. Wannek, I. Manke, H. Riesemeier, P. Krüger, J. Scholta, W. Lehnert, J. Banhart, and D. Stolten, "In-situ synchrotron X-ray radiography on high temperature polymer electrolyte fuel cells," *Electrochem. Commun.*, **12**, 1436 (2010).
22. P. Boillat, J. Biesdorf, P. Oberholzer, A. Kaestner, and T. J. Schmidt, "Evaluation of Neutron Imaging for Measuring Phosphoric Acid Distribution in High Temperature PEFCs," *J. Electrochem. Soc.*, **161**, 192 (2014).
23. F. Zhou, S. S. Araya, I. F. Grigoras, S. J. Andreasen, and S. K. Kær, "Performance Degradation Tests of Phosphoric Acid Doped Polybenzimidazole Membrane Based High Temperature Polymer Electrolyte Membrane Fuel Cells," *J. Fuel Cell Sci. Technol.*, **12**, 1 (2015).
24. W. Maier, T. Arlt, K. Wippermann, C. Wannek, I. Manke, W. Lehnert, and D. Stolten, "Correlation of Synchrotron X-ray Radiography and Electrochemical Impedance Spectroscopy for the Investigation of HT-PEFCs," *J. Electrochem. Soc.*, **159**, 398 (2012).
25. A. Weiss, S. Schindler, S. Galbiati, M. A. Danzer, and R. Zeis, "Distribution of Relaxation Times Analysis of High-Temperature PEM Fuel Cells Impedance Spectra," *Electrochimica Acta*, **230**, 391 (2017).
26. K. Kwon, J. O. Park, D. Y. Yoo, and J. S. Yi, "Phosphoric acid distribution in the membrane electrode assembly of high temperature proton exchange membrane fuel cells," *Electrochimica Acta*, **54**, 6570 (2009).
27. C. Wannek, I. Konradi, J. Mergel, and W. Lehnert, "Redistribution of phosphoric acid in membrane electrode assemblies for high-temperature polymer electrolyte fuel cells," *Int. J. Hy. Energy*, **34**, 9479 (2009).
28. S. Chevalier, M. Fazeli, F. Mack, S. Galbiati, I. Manke, A. Bazylak, and R. Zeis, "Role of the microporous layer in the redistribution of phosphoric acid in high temperature PEM fuel cells gas diffusion electrodes," *Electrochimica Acta*, **212**, 187 (2016).
29. N. Bevilacqua, M. G. George, S. Galbiati, A. Bazylak, and R. Zeis, "Phosphoric Acid Invasion in High Temperature PEM Fuel Cells Gas Diffusion Layers," *Electrochimica Acta*, **257**, 89 (2017).
30. S. H. Eberhardt, F. Marone, M. Stampanoni, F. N. Büchi, and T. J. Schmidt, "Imaging Phosphoric Acid Migration in High Temperature Polymer Electrolyte Fuel Cells by X-Ray Tomographic Microscopy," *ECS Trans.*, **69**, 591 (2015).
31. F. Marone and M. Stampanoni, "Regridding reconstruction algorithm for real-time tomographic imaging," *J. Synchrotron Radiat.*, **19**, 1029 (2012).
32. F. Marone, A. Studer, H. Billich, L. Sala, and M. Stampanoni, "Towards on-the-fly data post-processing for real-time tomographic imaging at TOMCAT," *Adv. Struct. Chem. Imaging*, **3**, 1 (2017).
33. R. Kuhn, J. Scholta, P. Krüger, C. Hartnig, W. Lehnert, T. Arlt, and I. Manke, "Measuring device for synchrotron X-ray imaging and first results of high temperature polymer electrolyte membrane fuel cells," *J. Power Sources*, **196**, 5231 (2011).
34. C. Simon, D. Kartouzian, D. Müller, F. Wilhelm, and H. A. Gasteiger, "Impact of Microporous Layer Pore Properties on Liquid Water Transport in PEM Fuel Cells: Carbon Black Type and Perforation," *J. Electrochem. Soc.*, **164**, F1697 (2017).
35. A. Suzuki, T. Hattori, R. Miura, H. Tsuboi, N. Hatakeyama, H. Takaba, M. C. Williams, and A. Miyamoto, "Porosity and Pt content in the catalyst layer of PEMFC: Effects on diffusion and polarization characteristics," *Int. J. Electrochem. Sci.*, **5**, 1948 (2010).
36. M. Sabharwal, L. M. Pant, A. Putz, D. Susac, J. Jankovic, and M. Secanell, "Analysis of Catalyst Layer Microstructures: From Imaging to Performance," *Fuel Cells*, **16**, 734 (2016).